Variable bandwidth, high efficiency microwave resonator for control of spin-qubits in nitrogen-vacancy centers

View Online   Export Citation   CrossMark

Anton Savitsky,[a] ID Jingfu Zhang, ID and Dieter Suter ID

AFFILIATIONS

Faculty of Physics, Technical University Dortmund, Otto-Hahn-Str. 4a, 44227 Dortmund, Germany

[a]Author to whom correspondence should be addressed: anton.savitsky@tu-dortmund.de. **Tel.:** +49-231-7558507

ABSTRACT

Nitrogen-Vacancy (NV) centers in diamond are attractive tools for sensing and quantum information. Realization of this potential requires effective tools for controlling the spin degree of freedom by microwave (mw) magnetic fields. In this work, we present a planar microwave resonator optimized for microwave-optical double resonance experiments on single NV centers in diamond. It consists of a piece of wide microstrip line, which is symmetrically connected to two 50 Ω microstrip feed lines. In the center of the resonator, an Ω-shaped loop focuses the current and the mw magnetic field. It generates a relatively homogeneous magnetic field over a volume of 0.07×0.1 mm^3. It can be operated at 2.9 GHz in both transmission and reflection modes with bandwidths of 1000 and 400 MHz, respectively. The high power-to-magnetic field conversion efficiency allows us to produce π-pulses with a duration of 50 ns with only about 200 and 50 mW microwave power in transmission and reflection, respectively. The transmission mode also offers capability for efficient radio frequency excitation. The resonance frequency can be tuned between 1.3 and 6 GHz by adjusting the length of the resonator. This will be useful for experiments on NV-centers at higher external magnetic fields and on different types of optically active spin centers.

Published under an exclusive license by AIP Publishing. https://doi.org/10.1063/5.0125628

I. INTRODUCTION

The nitrogen-vacancy (NV) center in diamond is used in various fields, such as quantum information, quantum sensing, magnetometry, and bioimaging.[1–5] In all applications, efficient manipulation of the electron spin is an essential prerequisite both for continuous wave (cw) experiments and for fast spin control in pulsed experiments. Therefore, maximizing the coupling between the control microwave (mw) magnetic field and the electron spins is a fundamental concern. Here, we consider specifically applications where single NV centers are excited by a laser and the spin state is read out by collecting photoluminescence (PL) through a microscope objective with large numerical aperture (NA > 1). Measuring a cw optically detected magnetic resonance (ODMR) spectrum requires a mw magnetic field of $H = 150$ A/m ($B = \mu_0 H = 0.19$ mT) to reach the maximum fluorescence contrast.[6] This field corresponds to a Rabi frequency of $f_R = 2$ MHz if the oscillating magnetic field is perpendicular to the NV axis. In pulsed experiments, typical π-pulse durations of $t_\pi = 50$ ns are used, which correspond to an excitation bandwidth

of $1.2/t_\pi = 24$ MHz ($f_R = 10$ MHz). This is sufficient for complete electron spin flip of the selected triplet spin transition.[6] This pulse length requires a magnetic field amplitude of $H = 800$ A/m.

Currently, most experimental setups rely on a wire positioned over the sample to achieve such mw magnetic field amplitudes. If this wire is placed in a short gap of a transmission line with $Z_L = 50$ Ω impedance, the electric current in the wire has an amplitude of $I = \sqrt{2P_{in}/Z_L} = 0.2$ A$/\sqrt{\text{W}} \cdot \sqrt{P_{in}}$. This current produces the tangential magnetic field $H_{wire} = \frac{I}{2\pi r}$ outside the wire of radius r_0. For a typical wire diameter of 20 μm, the maximum magnetic field generated at the wire surface is $H_{wire}(r_0) = 3200$ $\frac{A}{m}$ at 1 W of mw power. The wire is, however, optically opaque. Therefore, only NV-centers at a distance $> \sqrt{2}r_0$ from the center of the wire center can be optically probed. At this position, the magnetic field is reduced to 2600 $\frac{A}{m}$ at 1 W. Even at realistic distances from the wire of 40 μm, which still reduces the fluorescence collection efficiency due to obstruction by the wire, pulsed experiments can be performed with 1 W mw power, reaching $H_{wire}(40 \ \mu m) = 800$ $\frac{A}{m}$. Therefore, the microwire system is used in many laboratories, including our

laboratory.[7] A major disadvantage is that the $1/r$ dependence of the magnetic field amplitude significantly restricts the volume and the surface area available for probing single NV-centers and requires precise initial positioning of the microscope objective. Moreover, readjustment of the mw power settings is necessary for any new probed NV-center, which is not only due to the distance dependence of the magnetic field amplitude but also due to the magnetic field direction dependence on distance. This problem can be overcome using a microloop integrated into a transmission line instead of the microwire.[8,9] The magnetic field amplitude in the center of the ideal loop is given by $H_{loop} = \frac{I}{D}$, where D is the loop diameter. Thus, the field of 1000 $\frac{A}{m}$ can be generated by a loop with 200 μm diameter at 1 W mw power, which fulfills the requirements for ODMR. Advantages of the loop include a good homogeneity and directivity of the magnetic field over a $100 \times 100 \ \mu m^2$ area, much higher than the microwire. Compared to a wire, the loop magnetic field is, however, less tolerant to the effect of the metal case of the microscope objective, which must be positioned close to the sample. We discuss means to avoid this issue below.

There are several additional significant handicaps of loop, as well as wire, systems in conjunction with the transmission line: (i) the construction does not allow for quick replacement or reposition of the diamond specimen; (ii) significant heating effects (the resistance of the 10 mm copper wire with 20 μm diameter is 0.25 Ω at 3 GHz, which leads to power dissipation at the mw power level required for ODMR, but the thermal conductivity is limited due to the small conductor cross section); and (iii) substantial power return losses caused by the discontinuity in the transmission line. The main handicap is, however, the high mw powers required to fulfill the magnetic field requirements for ODMR experiments.

The power limitation can be overcome using planar resonators to generate the magnetic field. In the past, numerous reflection mode resonators were proposed based on different planar structures, for instance, double-split ring,[10,11] triple-split-ring,[12] loop-gap,[13] stripline,[14] and several other types.[15] All these resonators allow us to store the mw energy for a time proportional to the unloaded quality factor Q_0, which leads to the increase of the current and, therefore, an enhanced magnetic field amplitude proportional to $\sqrt{Q_0}$ as compared to a non-resonant structure with the same geometry. The resonator, however, introduces additional limitation. The substantial magnetic field enhancement is achieved only within the resonator bandwidth. For instance, a matched (critically coupled) reflection resonator with $Q_0 = 100$ would require 100× less mw power at the resonance frequency of $\nu_0 = 3$ GHz to generate the same mw magnetic field amplitude as compared to the non-resonant structure of the same geometry. This effect is, however, only obtained within $\Delta \nu_{1/2} = 2 \cdot Q_0^{-1} \cdot \nu_0 = 60$ MHz around the resonance frequency. This would substantially limit its general applicability for ODMR on single NV-centers. The bandwidth of a matched resonator can only be increased by lowering the Q_0-value.[13] This, however, leads to lower mw power to magnetic field conversion, i.e., it reduces the usefulness of the resonator.

The aim of this work is to develop a device that avoids these issues and can be used, e.g., for ODMR spectroscopy of single NV centers. It overcomes high power requirements and compromises limitations of transmission line systems and previously reported resonant structures. We design it to fulfill the following requirements: (i) easy and cost-effective fabrication with reliable resonator

parameters; (ii) compatibility with the standard coaxial mw delivery system; (iii) high mw power to magnetic field conversion efficiency; (iv) high magnetic field directivity and spatial homogeneity at least in the area accessible by nanopositioners based on the piezoelectric actuator ($100 \times 100 \ \mu m^2$); (v) small mw magnetic field frequency dependence, i.e., large bandwidth; (vi) possibility for microwave and radio frequency excitations; (vii) high mechanical and thermal stability; (viii) easy and reliable replacement or reposition of the diamond specimen; and (very important) (ix) compatibility with high resolution confocal objectives, i.e., tolerate the presence of dielectric and conductive parts in very close vicinity (200–300 μm) of the magnetic fields of the resonator.

II. RESULTS AND DISCUSSION

A. Resonator design

Figure 1 depicts the design of the developed half-wave resonator. It consists of a piece of wide microstrip line symmetrically connected to two 50 Ω microstrip feed lines terminated by SubMiniature version A (SMA) connectors. In the center of the microstrip, the Ω-loop concentrates the current and the mw magnetic field. The geometrical parameters of the resonator investigated in this study are summarized in the caption of Fig. 1. The diamond is placed on the loop, as shown in Fig. 1(b). Thus, the lower diamond surface is exposed to the mw magnetic field near the maximum amplitude. The resonator is fabricated using standard printed circuit board (PCB) lithography on a low loss Rogers RO3003 laminate with 166 μm overall thickness. This design allows us to explore the diamond up to least 100 μm above the surface. The resonator is designed for operation in transmission (the output SMA is terminated by a 50 Ω load) or reflection (the output SMA is open to free space) modes of operation.

B. Transmission mode resonator

Figure 2 shows the S-parameters of the resonator in the transmission mode calculated using CST Microwave Studio and measured experimentally using a network vector analyzer (HP 8720A).
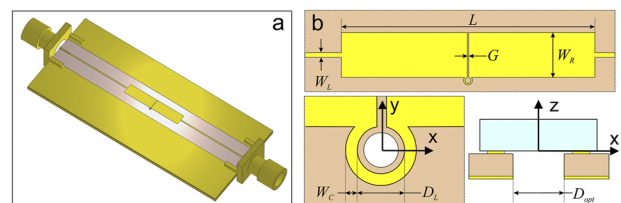

FIG. 1. (a) Full model of the microwave resonator. It is fabricated on a $60 \times 26 \ mm^2$ Rogers RO3003 low loss laminate ($\varepsilon_r = 3.00$, tan $\delta = 0.001$ at 10 GHz, dielectric thickness = 0.13 mm, and 18 μm copper cladding) mounted on a $60 \times 26 \times 1 \ mm^3$ copper holder and two standard PCB SMA flat tab connectors. (b) Resonator design. The geometrical parameters are as follows: $W_L = 0.3$ mm is the width of the microstrip feed line ($Z_L = 50 \ \Omega$), $W_R = 3$ mm is the width of the resonator, $L = 17$ mm is the length of the resonator, $G = 0.1$ mm is the gap width, $D_L = 0.4$ mm is the inner diameter of the loop, $W_C = 0.1$ mm is the width of the loop conductor, and $D_{opt} = 0.3$ mm is the diameter of the optical access hole. The coordinate system is indicated. For the optical pathway, see Fig. S8 of the supplementary material.
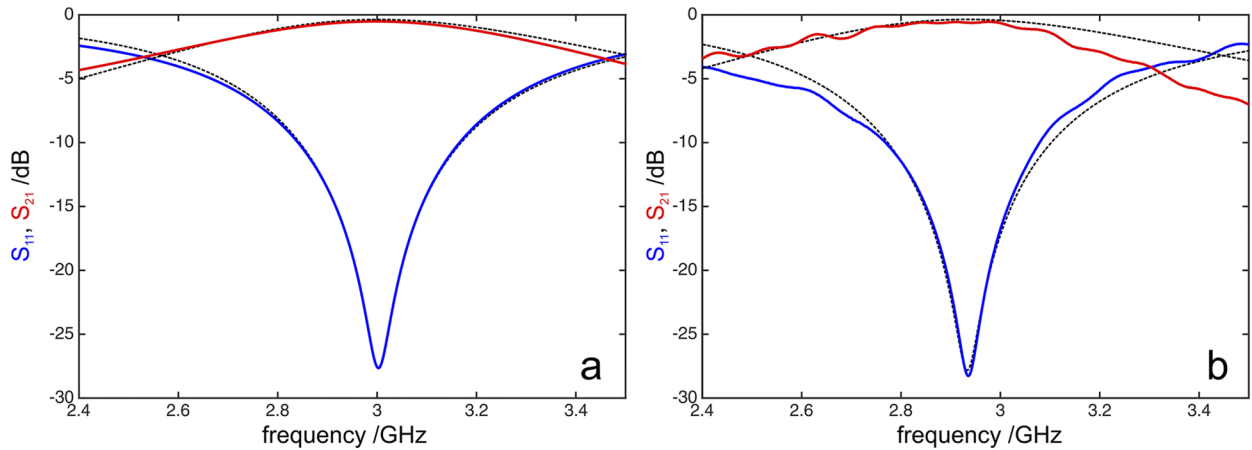
FIG. 2. (a) Simulated and (b) experimental S-parameters of the transmission resonator with diamond: $S_{11} = 20 \log_{10}|\Gamma|$ (blue line) and $S_{21} = 20 \log_{10}|T|$ (red line). The dashed lines show the best fit results of the S-curves to the reflection and transmission coefficients given by Eq. (1). The disagreement at the low and high frequencies is due to the frequency dependence of the characteristic impedances, which are not included in Eq. (1), and contributions from other resonator modes.

The analytical transmission and reflection coefficients of the symmetrically coupled transmission resonator with unloaded quality factor Q_0 and resonance frequency ν_0 are given by

$$\Gamma = -\frac{1 - i\xi}{1 + 2\beta - i\xi}, \qquad T = \frac{2\beta}{1 + 2\beta - i\xi}, \qquad (1)$$

where β is the coupling parameter for both input and output and $\xi = Q_0 \cdot \left(\frac{\nu_0}{\nu} - \frac{\nu}{\nu_0} \right)$ is the normalized offset.[16,17] Analysis of the S-parameter traces depicted in Fig. 2 using Eq. (1) yields the resonator parameters $Q_0 = 74$, $\beta = 11.5$ and $Q_0 = 73$, $\beta = 11.8$ for simulation and experiment, respectively. The relatively low unloaded quality factor is typical for microstrip based resonators owing to relatively high conduction losses.[18] The comparison of the calculated coupling parameter of 11.5 with $\beta = Q_0 \frac{Z_R}{Z_L} = 12.6$, which can be estimated analytically for the resonator, shows that the Ω-loop slightly increases the impedance of the resonator over the impedance of the microstrip line with width W_R (for more information, see the supplementary material). The central frequency of the experimental resonator was downshifted by about 70 MHz compared to the calculation. This deviation is ascribed to slightly different real parameters of the laminate (dielectric constant and thickness) and manufacturing tolerances.

The resonator itself is described by the coefficient $R^2 = 1 - |\Gamma|^2 - |T|^2$, i.e., the mw power transmitted to the resonator to which the magnetic field amplitude is proportional. This factor can be parameterized by the power coefficient at the resonance frequency and the resonator bandwidth,

$$R(\nu_0) = \frac{2\sqrt{\beta}}{1 + 2\beta}, \qquad \Delta\nu_{1/2} = \frac{1 + 2\beta}{Q_0} \cdot \nu_0. \qquad (2)$$

Thus, the bandwidth of the resonator is 950 and 990 MHz for the calculation and experiment, respectively, which is sufficient for most low-field applications of NV centers.

Figure 3 shows the spatial variation of the mw magnetic field behavior within the loop. At a small elevation above the loop surface ($z = 10$ μm), the loop provides a perfect magnetic field directivity over the optically accessible diamond area, i.e., the magnetic field is aligned with the z axis. At $z = 10$ μm, the position of the magnetic field minimum H (0, 70, 10 μm) = 1100 A/m is slightly shifted from the loop center due to the effect of the gap. The magnetic field amplitude increases by about a factor of 2 from the loop center to the edge of the optically accessible area. Above the loop, the decay of the magnetic field magnitude at the loop center is well described by the decay function for an ideal current loop,

$$H(0, 0, z) = H(0, 0, 0) \frac{D^3}{\left(4z^2 + D^2\right)^{\frac{3}{2}}} \qquad (3)$$

with $D = 440$ μm $> D_L$ due to the large width of the loop conductor ($W_c = D_L/4$); see Fig. 3(d). Below the loop, the magnetic field decays rapidly and is smaller than 70 A/m at the closest position of the microscope objective surface. This guarantees the stability of the system during operation as neither magnetic field distributions nor resonator parameters are influenced by the microscope objective. At higher elevation above the loop, the improvement of the magnetic field homogeneity is accompanied by slight loss of the field directivity; see Fig. S6 of the supplementary material. Within the optically accessible diamond area ($\pm x, \pm y, z$) = ($\pm 150, \pm 150, 0 + 100$) μm, the minimum and maximum of the magnetic field magnitude are 735 and 2200 A/m at 1 W mw power, respectively. Thus, the magnetic field of the loop compares very favorably with that of a microwire, in terms of both homogeneity and directivity.

C. Reflection mode resonator

The efficiency of the resonator can be improved by employing a reflection mode. The resonator is converted to the reflection mode by just disconnecting the output coax cable. The reflection resonator is given by
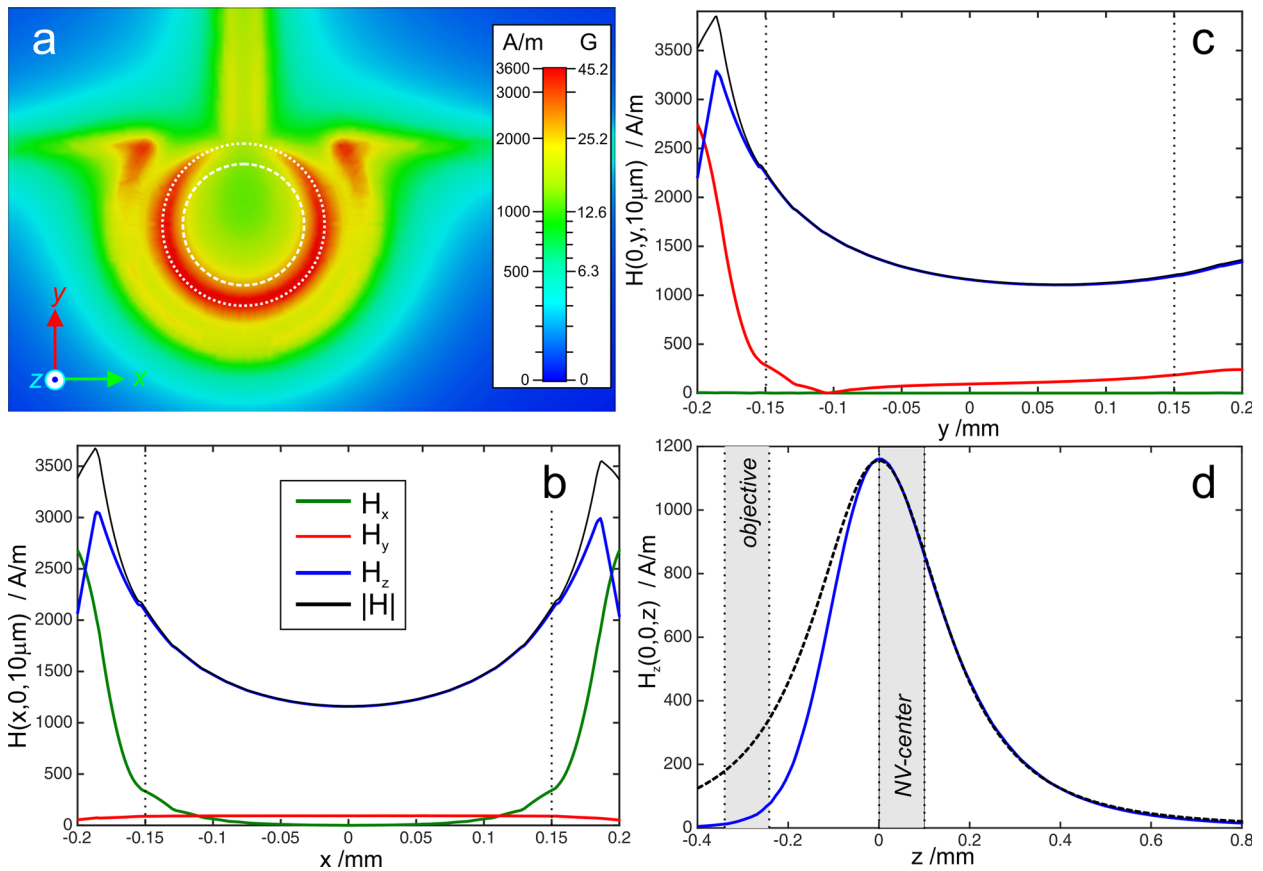
FIG. 3. (a) Color-coded plot of the calculated mw magnetic field magnitude, $|H|$, at $z = 10\ \mu m$ for a mw power of 1 W at the resonance frequency. The dotted and dashed circles mark the position of the inner loop edge ($D_L = 400\ \mu m$) and the optical access hole ($D_{opt} = 300\ \mu m$), respectively. (b)–(d) The H_x, H_y, H_z amplitudes of the mw magnetic field components as functions of the position x, y, z for a mw power of 1 W. The black dotted lines mark the optically accessible diamond area. The shadowed area in (d) shows the position region of the optical objective ($z < 0$) and NV-center ($z > 0$). The dashed lines in (d) show the best fit curve of $H_z(0, 0, z)$ to the function in Eq. (3).

$$R(v_0) = \frac{2\sqrt{\beta}}{1+\beta}, \quad \Delta v_{1/2} = \frac{1+\beta}{Q_0} \cdot v_0, \tag{4}$$

as derived from the reflection coefficient,[16]

$$\Gamma = -\frac{1-\beta-i\xi}{1+\beta+i\xi}. \tag{5}$$

Thus, for high coupling parameters, $\beta \gg 1$, the reflection mode offers a factor of 2 higher magnetic field amplitudes; see the supplementary material. The bandwidth, however, becomes reduced by a factor of 2. The magnetic field distribution in the loop area is identical in both resonator modes.

Figure 4 shows the calculated and experimental S_{11}-parameters of the resonator in the reflection mode. Analysis of the S-parameter traces using Eq. (5) yields the resonator parameters $Q_0 = 70$, $\beta = 8.3$ and $Q_0 = 60$, $\beta = 5.8$ for simulation and experiment, respectively. Thus, the bandwidth of the resonator is 400 and 320 MHz for calculation and experiment. The difference between transmission and

reflection modes and between calculated and experimental reflection parameters is mainly due to the open output line.

III. ODMR EXPERIMENTS

The mw magnetic field behavior was verified experimentally using a previously described ODMR setup capable for continuous wave and pulsed ODMR experiments; see Ref. 7 and the supplementary material. The $2 \times 2 \times 1\ mm^3$ diamond (001 cut) containing a 20 μm layer that was doped with NV centers was fixed to the resonator using transparent office tape; see Figs. S11 and S21 of the supplementary material. The central position of the optical objective was set close to the loop center.

Figure 5(a) shows a cw ODMR spectrum of the NV-centers located near the focal spot and recorded using a mw power of 6.8 mW (the power level was calibrated at 2.87 GHz). Two intense ODMR lines centered at 2.87 GHz are observed. The line splitting by 475 MHz corresponds to the external magnetic field component of
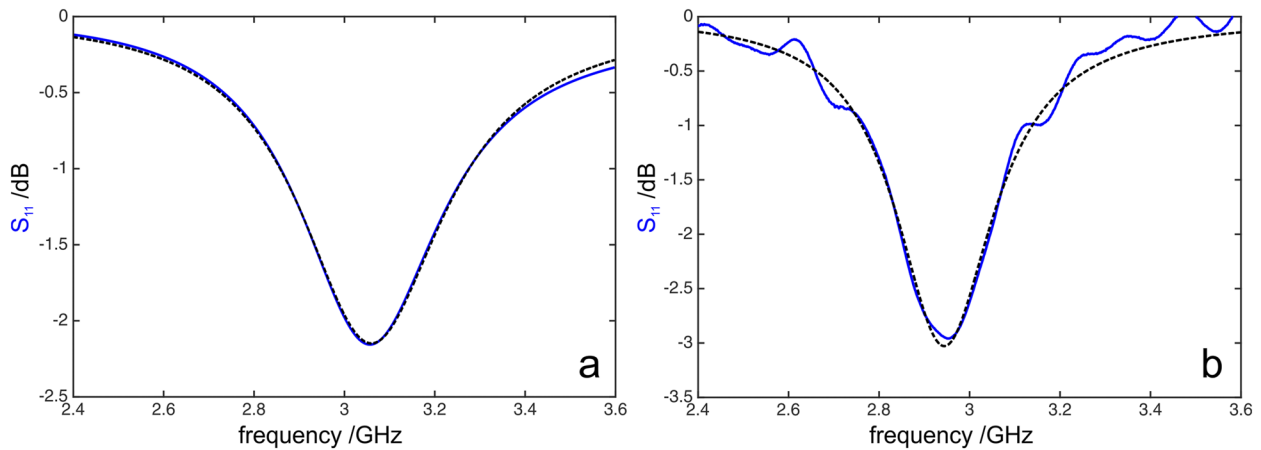
FIG. 4. Simulated (a) and experimental (b) S_{11}-parameters of the resonator operated in the reflection mode. The dashed line shows the best fit results of the S-curves to the reflection coefficient given by Eq. (5).

8.5 mT along the NV-axis. Additional ODMR line pairs with a splitting of 260, 160, and 60 MHz can be attributed to a set of NV-centers within the sensitive volume of about 300 nm in the x–y plane and 1000 nm in the z-direction (see Fig. S9 of the supplementary material). The different centers have different orientations along different [1,1,1] directions.

To measure the precise mw magnetic field strength, we recorded Rabi oscillations at the two strongest transitions, as shown in Fig. 5(b). The applied mw power of 680 mW resulted in a Rabi frequency of about 14 MHz. The Rabi frequency f_R is proportional to the magnetic field amplitude H,

$$f_R = \sqrt{\frac{2}{3}} \cdot \sqrt{2} \cdot \frac{\gamma_e}{2\pi} \frac{\mu_0 H}{2} = \frac{\gamma_e}{2\pi} \frac{\mu_0 H}{\sqrt{3}}, \tag{6}$$

where γ_e is the electron gyromagnetic ratio ($\gamma_e/2\pi$ = 28 GHz/T) and μ_0 is the permeability of the vacuum. The factor $\sqrt{2/3}$ accounts for the component of H that is perpendicular to the NV-axis, (mw H-axis parallel to [0,0,1] and NV-axis parallel to [1,1,1] crystal axis). The factor $\sqrt{2}$ takes into account that we drive one transition of the $S = 1$ spin. Thus, a Rabi frequency of f_R = 14 MHz at 0.68 W corresponds to a conversion efficiency of H = 840 $\frac{A}{m}$ at 1 W.
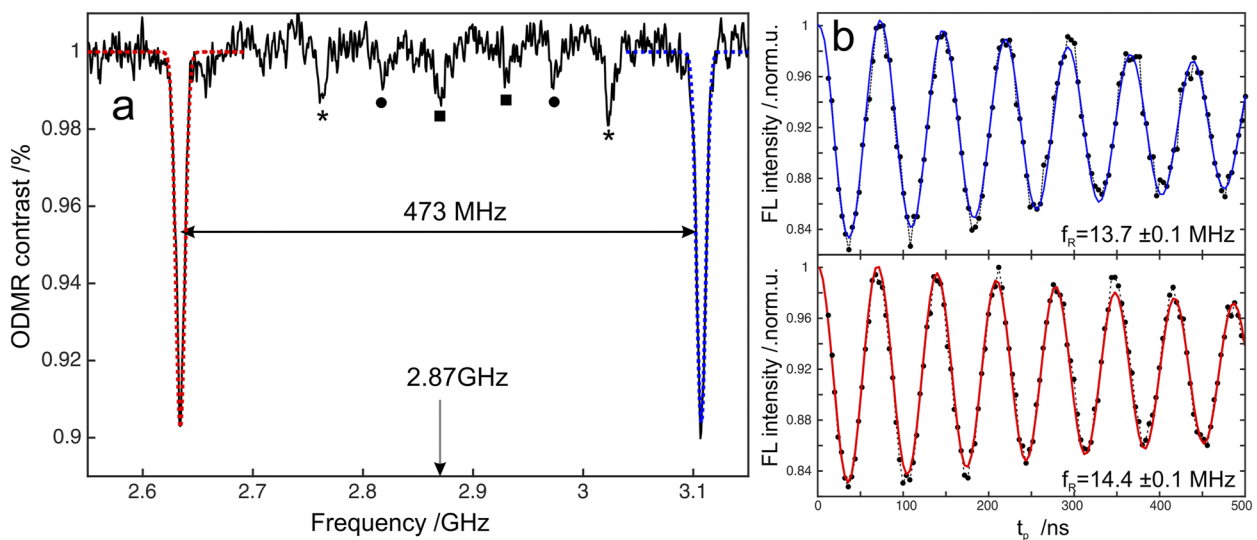

FIG. 5. (a) cw ODMR spectrum of the single NV-center at an external magnetic field alight close to [1,1,1] crystal axis recorded at 6.8 mW incident mw power. (b) The Rabi oscillation traces recorded at the mw frequencies of the high frequency [upper trace; marked blue in (a)] and low frequency [lower trace; red in (a)] ODMR lines and 680 mW mw power (+20 dB increased power over the cw experiment). The blue and red solid lines are the fits.
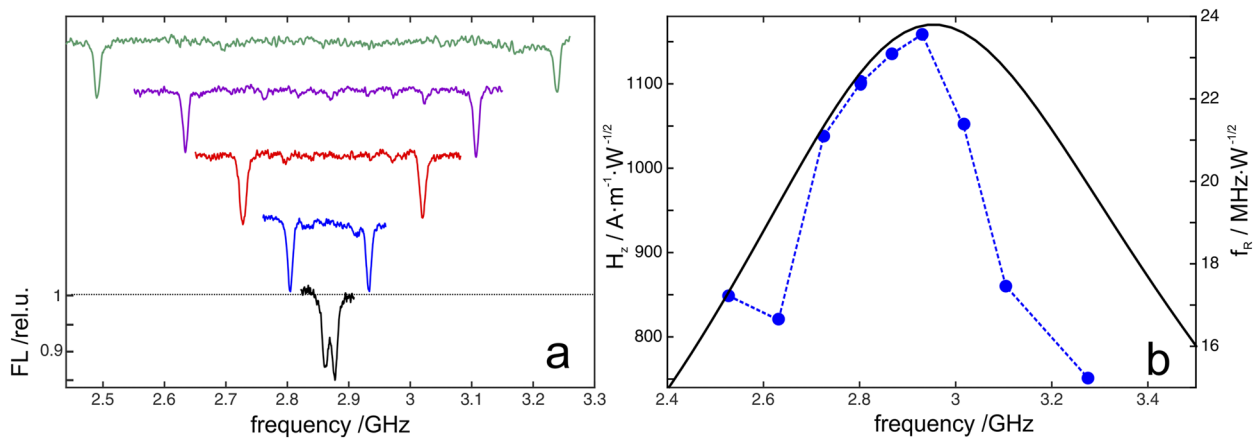
FIG. 6. (a) cw ODMR spectra of the single NV-center at different external magnetic fields at 6.8 mW incident mw power. (b) The frequency dependence of the magnetic field amplitude $H_z(0, 0, 10 \, \mu m)$ calculated for the transmission resonator (black curve, left scale). Rabi nutation frequencies (dots, right scale) evaluated from experimental Rabi oscillation traces recorded at the ODMR line positions in (a). The Rabi frequencies are normalized to 1 W mw power calibrated at 2.87 GHz. The left and right scales are adjusted according to Eq. (6).

In the next step, the cw and pulsed ODMR experiments were performed at different external magnetic fields and the same input power of the mw amplifier; see Fig. 6(a). The magnetic field amplitude evaluated from the Rabi frequencies overlaid with the simulation results is depicted in Fig. 6(b). Both curves are in the good agreement. The variation of the mw magnetic field over a frequency range of 800 MHz is less than 40%. The discrepancy at the frequencies above 3 GHz is attributed to the gain variation of the high-power mw amplifier operated below saturation. The spatial distribution of H in the x–y plane was evaluated from the Rabi experiment at 2.93 GHz for ten different NV centers over the area of $70 \times 70 \, \mu m^2$ accessible by the nanopositioner. The variation of the magnetic field

of less than 20% (1000 to 1250 A/m) is in good agreement with simulation predictions.

These results show that the transmission resonator achieves good spatial magnetic field homogeneity and the bandwidth required for most ODMR experiments on single NV-centers. The transmission resonator achieves π-pulse durations of 20 ns (f_R = 25 MHz) using about 1 W mw power. For this performance, a mw amplifier is required. This limitation can be overcome by operating the resonator in the reflection mode.

Figure 7(a) shows the Rabi nutation traces recorded at the high frequency ODMR line at 2.93 GHz with 680 mW input mw power. The upper trace was acquired using the resonator in the
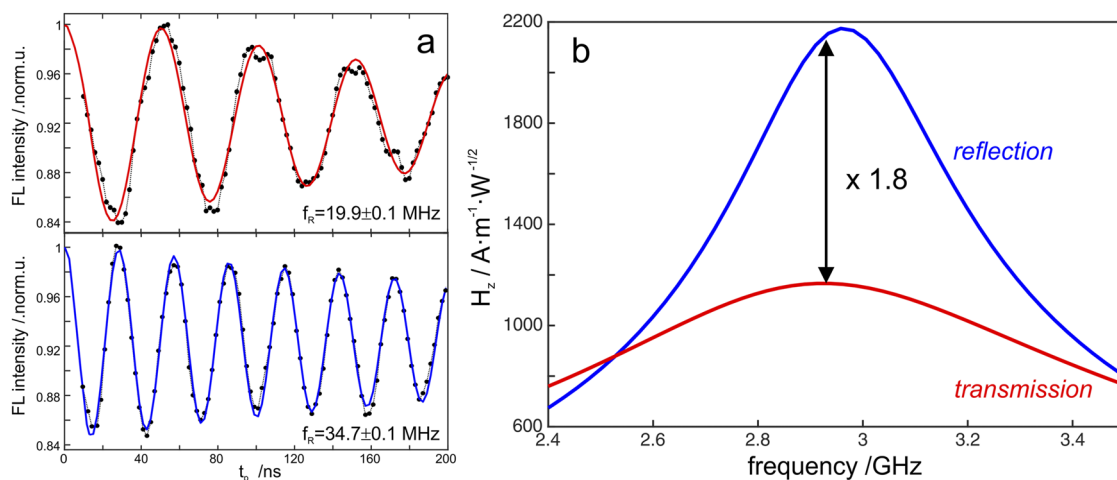

FIG. 7. (a) Rabi oscillation traces recorded at the mw frequency 2.93 GHz for the resonator in transmission (upper trace) and reflection (lower trace) modes at 680 mW mw power. The traces were acquired subsequently at the same settings with the output cable connected and disconnected. The solid-colored lines are the fits. (b) Frequency dependence of the magnetic field amplitude $H_z(0, 0, 10 \, \mu m)$ calculated for the transmission (red trace) and reflection resonator (blue trace). The amplitude ratio at 2.93 GHz is indicated by the arrow.

transmission mode. Subsequently, the output mw cable was disconnected converting the resonator into the reflection mode, and the lower trace was acquired. The magnetic field amplitudes evaluated from Rabi frequencies are 1190 and 2070 A/m for transmission and reflection settings, respectively. The experimentally observed increase of the resonator efficiency by a factor of 1.74 is in good agreement with factor 1.8 obtained from calculation; see Fig. 7(b). Thus, the reflection resonator is capable of producing the same magnetic field amplitude using about a factor of 3 smaller mw power. It achieves 20 ns π-pulses (f_R = 25 MHz) with as little as 300 mW mw power.

At this point, we put two remarks: (i) The highest f_R achieved in our setup allows us to realize π-pulses with 7 ns duration and 4 ns in transmission and reflection modes, respectively. The pulse profile of such short pulses is not distorted by the resonator, neither in transmission nor in reflection mode, since their voltage ringing times are $t_r = \frac{1}{\pi \Delta \nu_{1/2}}$ = 0.3 ns and 1 ns, respectively. (ii) The performance of the microscope objective employed in this work, in particular the efficiency of fluorescence collection, is restricted by the resonator acting as an optical diaphragm; see the supplementary material. Despite this restriction, the collection of high quality ODMR data is still possible within reasonable time.

IV. PERFORMANCE SUMMARY

The goal of this work was the design of a device for efficient control of spin qubits. For optimal performance, it should have a number of properties that we specified in the Introduction. Here, we first summarize the quantitative performance measures of the mw and rf properties, as shown in Table I; the values shown were calculated and verified by experiments. For comparison, it also includes the parameters calculated for the 50 Ω microstrip transmission line with the same Ω-type loop. The resonator offers factors of 4.8 (transmission) and 9.1 (reflection) higher magnetic field amplitudes at the same input mw power as compared to the transmission line. Pulsed ODMR experiments with reasonably short π-pulses of 50 ns can be generated using only 50 mW mw power with the resonator operated in the reflection mode. Thus, it allows us to avoid high-power mw amplification stages or even to perform the experiments directly using the output of a mw generator. The transmission mode is more advantages for experiments at higher external magnetic fields owing to the larger resonator bandwidth. In contrast to the reflection mode, it allows us to the perform experiments with combined microwave and radio frequency excitations. An additional

advantage of the transmission mode is the good matching of the resonator input. The input return losses are ≤20 dB (±50 MHz) and ≤10 dB (±150 MHz) around the resonance frequency; see Fig. 2. Thus, in contrast to the reflection resonator, the mw excitation system does not require matching elements (circulator or attenuator) on the input for ODMR experiments at small external magnetic fields.

We also considered heating effects. Conduction losses in the loop can lead to a temperature increase that can potentially influence the experiment. The thermal analysis of the transmission mode resonator at ambient temperature shows that the temperature increase in the loop-diamond region is <0.3 K for 0.1 W continuous mw power (see Fig. S3 of the supplementary material). At this mw power, the produced magnetic field of 370 A/m corresponds to a Rabi frequency f_R = 7.5 MHz, which is more than sufficient for cw ODMR detection with the highest contrast.[6] In pulsed ODMR experiments, the average heat power is significantly smaller. The transmission resonator allows for above 10^6 π-pulses at 10 W (t_π = 7 ns) with no significant heating effects. The results of the thermal analysis are consistent with experimental observations.

The resonator design can be adapted for experiments on NV-centers at higher external magnetic fields or different types of optically active spin centers by adjusting some of the design parameters. The variation of the overall resonator length, L, between 5 and 56 mm allows us to tune the resonance frequency between 6 and 1.3 GHz without significant loss of the mw performance; see Fig. S16 of the supplementary material. Further increasing or decreasing the resonance frequency is possible by adjusting the dielectric constant and thickness of the substrate and the geometry of the holder.

Various types of microwave resonators have been proposed for experiments on optically active spin centers, such as the diamond NV center, each with specific advantages and limitations. A fair comparison of the performance of all these different designs would have to be made under a specific set of conditions, where all designs can operate. Since this is not possible, we include here a comparison with two recently reported designs with overlapping boundary conditions, which are applied in several laboratories for experiments on NV-centers.[10,11,13,19–26] The first system, originally reported by Bayat et al.,[10] is based on a double-split-ring resonator operated in reflection. The original design has an efficiency of 355 A/m/$\sqrt{W}$ with a bandwidth of 40 MHz. Similar numbers were reported for some modified designs.[11,25] The second design, originally reported by Sasaki et al.,[13] is based on a split-ring (or loop-gap) resonator in the reflection. The original design provides 240 A/m/$\sqrt{W}$

TABLE I. Summary of resonator and transmission line performances.

Case	$H_{MW}/\sqrt{P_{in}}$ (A/m/$\sqrt{W}$)	P_{in}[a] (W)	$\Delta \nu_{1/2}$ (MHz)	$H_{RF}/\sqrt{P_{in}}$[b] (A/m/$\sqrt{W}$)
Transmission line	245[c]	4.0	Full	252 (252)
Transmission resonator	1170[d]	0.18	950	265 (266)
Reflection resonator	2230[d]	0.05	400	10 (160)

[a]Input mw power required for the 50 ns π-pulse (f_R = 10 MHz) and NV-center in a 001 diamond.
[b]Calculated at 10 MHz (200 MHz).
[c]Calculated at 2.9 GHz.
[d]Calculated at the resonance frequency (~2.9 GHz).

with a bandwidth of 440 MHz. Better parameters 485 A/m/$\sqrt{W}$ and 300 MHz are reported for the modified version.[20] Thus, the performance of our system in both transmission and reflection modes of operation is superior to both systems.

V. CONCLUSION

In this work, we presented a novel mw excitation system based on a resonator designed for cw and pulsed ODMR experiments on single NV-centers to be combined with confocal microscopy. The high performance of the system was verified using numerical EM calculations and ODMR experiments. The resonator can be easily and cost-effectively fabricated using standard PCB lithography. It offers high mechanical and thermal stability. Its performance in terms of mw power to magnetic field conversion efficiency and magnetic field homogeneity is superior in comparison to currently used systems, such as the microwire-transmission line system. It also offers a range of practical advantages, such as simplified optical adjustment and optimization of the mw power settings for all types of ODMR experiments. It also offers the possibility for the quick replacement of the diamond crystal because it does not have to be permanently connected to the resonator. This provides the opportunity for the investigation of different samples with the same structure or use a resonator, which is optimized for the performance of a specific type of ODMR experiment.

While the present work focuses on applications on NV centers in diamond, the principles used here are completely general and can be readily transferred to similar systems that rely on efficient spin control by microwave fields. This includes not only ensembles of NV centers but also other materials, such as semiconductors.

SUPPLEMENTARY MATERIAL

See the supplementary material for the optimization of the resonator parameters, radio frequency performance, fluorescence collection efficiency, experimental details, and frequency tuning capability and also the resonator layouts in Gerber and DXF formats.

ACKNOWLEDGMENTS

AUTHOR DECLARATIONS

Conflict of Interest

The authors have no conflicts to disclose.

Author Contributions

Anton Savitsky: Conceptualization (equal); Formal analysis (lead); Investigation (equal); Methodology (lead); Visualization (lead); Writing – original draft (lead). **Jingfu Zhang**: Data curation (equal); Formal analysis (equal); Investigation (equal). **Dieter Suter**: Conceptualization (equal); Funding acquisition (lead); Writing – review & editing (equal).

DATA AVAILABILITY

The data that support the findings of this study are available from the corresponding author upon reasonable request.

REFERENCES

[1]D. Suter and F. Jelezko, Prog. Nucl. Magn. Reson. Spectrosc. **98–99**, 50–62 (2017).
[2]J. Wrachtrup and F. Jelezko, J. Phys.: Condens. Matter **18**(21), S807–S824 (2006).
[3]M. W. Doherty, N. B. Manson, P. Delaney, F. Jelezko, J. Wrachtrup, and L. C. L. Hollenberg, Phys. Rep. **528**(1), 1–45 (2013).
[4]J. F. Barry, J. M. Schloss, E. Bauch, M. J. Turner, C. A. Hart, L. M. Pham, and R. L. Walsworth, Rev. Mod. Phys. **92**(1), 015004 (2020).
[5]G. Balasubramanian, A. Lazariev, S. R. Arumugam, and D.-w. Duan, Curr. Opin. Chem. Biol. **20**, 69–77 (2014).
[6]A. Dréau, M. Lesik, L. Rondin, P. Spinicelli, O. Arcizet, J.-F. Roch, and V. Jacques, Phys. Rev. B **84**(19), 195204 (2011).
[7]J. Zhang, J. H. Shim, I. Niemeyer, T. Taniguchi, T. Teraji, H. Abe, S. Onoda, T. Yamamoto, T. Ohshima, J. Isoya, and D. Suter, Phys. Rev. Lett. **110**(24), 240501 (2013).
[8]P. L. Stanwix, L. M. Pham, J. R. Maze, D. Le Sage, T. K. Yeung, P. Cappellaro, P. R. Hemmer, A. Yacoby, M. D. Lukin, and R. L. Walsworth, Phys. Rev. B **82**(20), 201201 (2010).
[9]O. R. Opaluch, N. Oshnik, R. Nelz, and E. Neu, Nanomaterials **11**(8), 2108 (2021).
[10]K. Bayat, J. Choy, M. Farrokh Baroughi, S. Meesala, and M. Loncar, Nano Lett. **14**(3), 1208–1213 (2014).
[11]N. Zhang, H. Yuan, C. Zhang, L. Xu, J. Zhang, G. Bian, B. Li, and J. Fang, Appl. Phys. Express **11**(8), 086602 (2018).
[12]Z. Ma, D. Zheng, Y. Fu, H. Yuan, W. Guo, J. Zhao, B. Li, Y. Shi, X. Zhang, and J. Liu, Jpn. J. Appl. Phys. **58**(5), 050919 (2019).
[13]K. Sasaki, Y. Monnai, S. Saijo, R. Fujita, H. Watanabe, J. Ishi-Hayase, K. M. Itoh, and E. Abe, Rev. Sci. Instrum. **87**(5), 053904 (2016).
[14]Y. S. Yap, M. Negoro, M. Kuno, Y. Sakamoto, A. Kagawa, and M. Kitagawa, J. Phys. Soc. Jpn. **91**(4), 044004 (2022).
[15]G. Mariani, S. Nomoto, S. Kashiwaya, and S. Nomura, Sci. Rep. **10**(1), 4813 (2020).
[16]M. C. Sanchez, E. Martin, and J. M. Zamarro, IEE Proc., Part H: Microwaves, Opt. Propag. **137**(4), 209–212 (1990).
[17]J. L. Altman, *Microwave Circuits* (Van Nostrand, New York, 1964).
[18]A. Gopinath, IEEE Trans. Microwave Theory Tech. **29**(2), 128–131 (1981).
[19]M. Tsukamoto, K. Ogawa, H. Ozawa, T. Iwasaki, M. Hatano, K. Sasaki, and K. Kobayashi, Appl. Phys. Lett. **118**(26), 264002 (2021).
[20]V. K. Sewani, H. H. Vallabhapurapu, Y. Yang, H. R. Firgau, C. Adambukulam, B. C. Johnson, J. J. Pla, and A. Laucht, Am. J. Phys. **88**(12), 1156–1169 (2020).
[21]S. Nomura, K. Kaida, H. Watanabe, and S. Kashiwaya, J. Appl. Phys. **130**(2), 024503 (2021).
[22]G. Mariani, A. Umemoto, and S. Nomura, AIP Adv. **12**(6), 065321 (2022).
[23]P. Reuschel, M. Agio, and A. M. Flatae, Adv. Quantum Technol. **5**(11), 2200077 (2022).
[24]M. Tsukamoto, S. Ito, K. Ogawa, Y. Ashida, K. Sasaki, and K. Kobayashi, Sci. Rep. **12**(1), 13942 (2022).
[25]F. M. Stürner, A. Brenneis, T. Buck, J. Kassel, R. Rölver, T. Fuchs, A. Savitsky, D. Suter, J. Grimmel, S. Hengesbach, M. Förtsch, K. Nakamura, H. Sumiya, S. Onoda, J. Isoya, and F. Jelezko, Adv. Quantum Technol. **4**(4), 2000111 (2021).
[26]N. Zhang, H. Yuan, C. Zhang, L. Xu, J. Zhang, G. Bian, P. Fan, H. Yuan, and J. Fang, IEEE Sens. J. **19**(2), 451–456 (2019).

Anton Savitsky, Jingfu Zhang and Dieter Suter

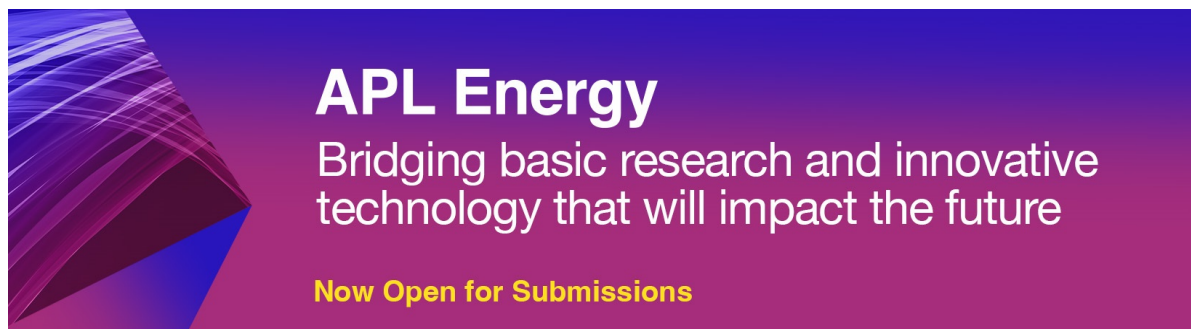View Online   Export Citation   CrossMark

APL Energy
Bridging basic research and innovative technology that will impact the future
Now Open for Submissions